

The Stellar Kinematics of Void Dwarf Galaxies Using KCWI

MITHI A. C. DE LOS REYES,^{1,2} EVAN N. KIRBY,³ ZHUYUN ZHUANG,⁴ CHARLES C. STEIDEL,⁴ YUGUANG CHEN,⁵ AND CORAL WHEELER⁶

¹*Department of Physics, Stanford University, 382 Via Pueblo Mall, Stanford, CA 94305, USA*

²*Kavli Institute for Particle Astrophysics & Cosmology, P.O. Box 2450, Stanford University, Stanford, CA 94305, USA*

³*Department of Physics & Astronomy, University of Notre Dame, 225 Nieuwland Science Hall, Notre Dame, IN 46556, USA*

⁴*Department of Astronomy, California Institute of Technology, 1200 E. California Blvd., Pasadena, CA 91125, USA*

⁵*Department of Physics & Astronomy, University of California Davis, 1 Shields Ave, Davis, CA 95616, USA*

⁶*Department of Physics & Astronomy, California State Polytechnic University Pomona, 3801 West Temple Avenue, Pomona, CA 91768, USA*

Submitted to ApJ

ABSTRACT

Dwarf galaxies located in extremely under-dense cosmic voids are excellent test-beds for disentangling the effects of large-scale environment on galaxy formation and evolution. We present integral field spectroscopy for low-mass galaxies ($M_{\star} = 10^7 - 10^9 M_{\odot}$) located inside ($N = 21$) and outside ($N = 9$) cosmic voids using the Keck Cosmic Web Imager (KCWI). Using measurements of stellar line-of-sight rotational velocity v_{rot} and velocity dispersion σ_{\star} , we test the tidal stirring hypothesis, which posits that dwarf spheroidal galaxies are formed through tidal interactions with more massive host galaxies. We measure low values of $v_{\text{rot}}/\sigma_{\star} \lesssim 2$ for our sample of isolated dwarf galaxies, and we find no trend between $v_{\text{rot}}/\sigma_{\star}$ and distance from a massive galaxy $d_{L^{\star}}$ out to $d_{L^{\star}} \sim 10$ Mpc. These suggest that dwarf galaxies can become dispersion-supported “puffy” systems even in the absence of environmental effects like tidal interactions. We also find indications of an upward trend between $v_{\text{rot}}/\sigma_{\star}$ and galaxy stellar mass, perhaps implying that stellar disk formation depends on mass rather than environment. Although some of our conclusions may be slightly modified by systematic effects, our main result still holds: that isolated low-mass galaxies may form and remain as puffy systems rather than the dynamically cold disks predicted by classical galaxy formation theory.

1. INTRODUCTION

Galaxies are not closed systems. Not only do they affect their surroundings—through, e.g., outflows of gas—but their evolution is often affected by their immediate environments. Low-mass “dwarf” galaxies¹ are thought to be particularly susceptible to environmental effects. Due to their small gravitational potential wells, they tend to be more strongly influenced by outflows of metal-enriched gas (or inflows of pristine gas) and are therefore more metal-poor than massive galaxies (Tremonti et al. 2004).

One way to disentangle the effect of environment in galaxy evolution is to study systems in which potential environmental effects are minimized. This requires looking beyond our own neighborhood: even the handful of currently-known Local Group dwarf galaxies that are relatively isolated (i.e., not clearly associated with either the Milky Way or M31) are still within ~ 1 Mpc of the nearest L^{\star} galaxy² (McConnachie et al. 2021). Even the most distant dwarf galaxies in the Local Group could be “backsplash galaxies” that may have interacted with an L^{\star} host in the past (Teyssier et al. 2012). We instead search for dwarf galaxies in the lowest-density environments in the universe: cosmic voids. The vast majority of the matter in the universe resides in filaments in the so-called “cosmic web” (Bond et al. 1996), but galaxies

Corresponding author: Mithi A. C. de los Reyes
mdlreyes@stanford.edu

¹ The definition of “dwarf” galaxies can vary significantly; here, we consider “classical” dwarf galaxies with stellar masses $< 10^9 M_{\odot}$.

² L^{\star} galaxies are approximately Milky Way-mass galaxies; throughout this work we adopt a relatively conservative definition of L^{\star} galaxies as galaxies with stellar masses $M_{\star} > 10^{10} M_{\odot}$.

can still be found in the large ($\gtrsim 10$ Mpc) and underdense ($\rho_{\text{void}} \sim 0.1\rho_{\text{avg}}$) voids between filaments. Dwarf galaxies in these cosmic voids can be located $\gtrsim 5$ Mpc from other galaxies—perhaps as far removed from the external influences of other galaxies as possible in the local universe—making them an ideal population for observing how galaxies evolve in near-total isolation.

Furthermore, Λ CDM predicts that the evolution of void galaxies will be slowed relative to “field” galaxies located in cosmic filaments, due to longer timescales between galaxy-galaxy interactions (Goldberg & Vogeley 2004). Indeed, most void dwarfs appear to be optically blue, compact, and actively star forming, suggesting that they are less evolved than their field counterparts (e.g., Kreckel et al. 2012; Grogin & Geller 2000, 1999). This may make void dwarf galaxies useful analogs to the high-redshift galaxies that were the building blocks for Milky Way-like galaxies. Detailed characterizations of high- z analogs in the local universe might provide complementary information to direct high- z observations taken by, e.g., JWST (Gardner et al. 2006).

A number of previous studies have aimed to characterize the galaxies located in voids (e.g., Pustilnik et al. 2011, 2016; Pustilnik et al. 2019; Kreckel et al. 2012, 2014; Penny et al. 2015; Beygu et al. 2016, 2017; Douglass & Vogeley 2017; Kniazev et al. 2018; Wegner et al. 2019; Florez et al. 2021; Domínguez-Gómez et al. 2022, and references therein). However, the vast majority of these studies have aimed to measure integrated galaxy properties, including global colors, star formation rates, and metallicities. This paper describes an observational program designed to measure the *spatially-resolved* properties of a sample of local void dwarf galaxies. In particular, this program aims to probe the stellar kinematics of these galaxies, which can help shed light on the dynamical processes that drive galaxy formation.

Classical galaxy formation theory suggests that all galaxies form as thin, rotationally supported disks (White & Rees 1978; Fall & Efstathiou 1980; Mo et al. 1998). However, it is not clear whether this picture of disk formation extends to dwarf galaxies ($M_{\star} \lesssim 10^9 M_{\odot}$). Disk-like morphologies are not as readily apparent among dwarf galaxies, particularly compared to the obvious and dramatic spiral disks common among higher-mass galaxies, leading some authors to suggest that dwarf and disk galaxies are structurally distinct systems (Schombert 2006). Detailed kinematic measurements are most readily available for the dwarf galaxies closest to us: our own Local Group. The Local Group hosts both gas-rich star-forming dwarf irregular (dIrr) galaxies and gas-poor dwarf spheroidal (dSph) galaxies (e.g., McConnachie 2012). The prevalence of

these two classes is a well-known function of location: most dIrrs live outside the virial radii of the Milky Way or M31, while satellite galaxies are typically dSphs. This local “morphology-density relation” (first noted by Einasto et al. 1974) appears to be a direct consequence of environmental effects, as tides and ram-pressure stripping can remove gas from gas-rich dIrrs and turn them into gas-poor dSphs (e.g., Grcevich & Putman 2009; Spekkens et al. 2014; Putman et al. 2021).

Environmental effects have also been thought to affect the stellar kinematics of Local Group dwarf galaxies. In the “tidal stirring” model (Mayer et al. 2001), a rotationally supported dwarf galaxy with a stellar disk will experience repeated tidal shocks as it passes through the pericenter of its orbit around a massive host galaxy. These shocks may produce a tidally induced bar, which transfers angular momentum to the outer regions of the galaxy. As high-angular momentum material is stripped, the overall rotation of the galaxy decreases, transforming it into a pressure-supported, kinematically “puffy” stellar system. Simulations have had some success in showing that dSphs may be formed from dIrrs through this mechanism (e.g., Kazantzidis et al. 2017, and references therein).

Yet the kinematic distinction between dIrrs and dSphs is perhaps more ambiguous than the tidal stirring model would suggest. Stellar spectroscopy has revealed that a number of Local Group dIrrs are primarily dispersion-supported (e.g., Leaman et al. 2012; Kirby et al. 2017)—and indeed, nearly all the lowest-mass ($M_{\star} \lesssim 10^8 M_{\odot}$) Local Group dwarf galaxies are either dispersion-supported or only weakly rotationally supported (Kirby et al. 2014; Wheeler et al. 2017). Wheeler et al. (2017) suggested that this may point to a formation scenario in which dwarf galaxies initially form as “puffy” stellar systems rather than dynamically cold disk systems, and they show that zoom-in simulations of isolated dwarf irregular galaxies are consistent with this picture. In this paper, we demonstrate that void dwarf galaxies provide a useful test of these scenarios.

The structure of this paper is as follows. We describe the observations and data reduction in Section 2. In Section 3, we present measurements of spatially-resolved stellar kinematics, before discussing the implications of these results in Section 4. We summarize our conclusions in Section 5.

2. DATA

Since the stellar populations of galaxies outside the Local Group cannot be resolved, spatially-resolved spectroscopy is needed to estimate stellar kinematic properties. While long-slit spectroscopy can be used to ob-

tain measurements along single axes, integral field units (IFUs) can obtain spectral information across the full spatial extent of an extended source. We used the Keck Cosmic Web Imager (KCWI; [Morrissey et al. 2018](#)) on the Keck II telescope to obtain IFU observations of dwarf galaxies inside and outside voids. In this section, we describe the sample selection, observations, and data reduction process.

2.1. Sample selection

We selected a sample of void dwarf galaxies from Table 1 of [Douglass et al. \(2018\)](#), who identified 993 void dwarf galaxies from the Sloan Digital Sky Survey Data Release 7 (SDSS DR7; [Abazajian et al. 2009](#)). To classify these galaxies as “void” galaxies, [Douglass et al. \(2018\)](#) used the void catalog compiled by [Pan et al. \(2012\)](#), which was built from the SDSS DR7 catalog using the VoidFinder algorithm ([Hoyle & Vogeley 2002](#); [El-Ad & Piran 1997](#)). This algorithm finds geometric voids using the spatial distribution of massive galaxies in SDSS DR7 (with absolute magnitudes $M_r < -20$). Isolated galaxies (described as having the third nearest-neighbor more than ~ 7 Mpc/ h away) are removed, then all remaining “wall” galaxies are placed on a three-dimensional grid. Every grid cell devoid of “wall” galaxies is potentially part of a void, so VoidFinder aims to identify the maximal sphere that can be drawn in the void: a sphere is grown from each empty grid cell, reaching its maximum size once four galaxies are present on its surface (since a sphere is uniquely defined by four non-coplanar points). Overlapping spheres are combined, and any sphere with radius > 10 Mpc is then associated with a void.

We chose 19 void dwarf galaxies, aiming to evenly span a range of stellar masses from $10^7 - 10^9 M_\odot$ (i.e., approximately one galaxy in each 0.1 dex stellar mass bin). Because gas-phase metallicities are a property of particular interest in void dwarf galaxies (e.g., [Kreckel et al. 2014](#); [Douglass & Vogeley 2017](#); [Pustilnik et al. 2016](#)), we further prioritized galaxies in each mass bin with the highest [OIII] λ 4363 fluxes.³ These preliminary parameters used in our sample selection were obtained from the SDSS value-added catalogs: stellar masses were estimated using the star-forming Portsmouth ([Maraston 2005](#)) method, which fit stellar evolution models to SDSS photometry, while the emission line fluxes were obtained from the MPA/JHU value-added catalog ([Tremonti et al. 2004](#)). We note that these parameter estimates are only used for target selection, and we

compute independent stellar masses from mid-infrared photometry later in our analysis (Section 4.2).

By targeting galaxies selected from geometric voids in a galaxy survey, this sample selection implicitly assumes that the relatively bright ($m_r < 17.77$) galaxies in SDSS DR7 perfectly trace the underlying dark matter distribution of the universe. This may not be the case (see [Desjacques et al. 2018](#), for a review of galaxy bias), which means our void sample could be contaminated with galaxies that are not in truly low-density voids—that is, galaxies that live in regions devoid of relatively bright galaxies, but which still contain “dark” non-emitting gas, ultra low surface brightness systems, or dark matter. While a full investigation of this selection is beyond the scope of this paper, we are able to confirm that these void galaxies are at least extremely isolated from massive host galaxies (Section 4.1).

An additional 7 dwarf galaxies were also selected from SDSS Data Release 16 (SDSS DR16; [Ahumada et al. 2020](#)) as a control sample, with stellar masses similar to those of galaxies in the void sample. These were selected to have relatively low redshift ($z < 0.02$), visible [OIII] and $H\beta$ lines in their SDSS spectra, and (as with the void galaxies) were prioritized based on their [OIII] λ 4363 flux. These control galaxies were either observed or identified as galaxies in SDSS data releases after DR7, so they could not be directly checked against the SDSS DR7 void catalog of [Pan et al. \(2012\)](#). Given the relative rarity of void dwarf galaxies—[Douglass et al. \(2018\)](#) identified 993/9519 (10%) of the SDSS DR7 dwarf galaxies as “void” galaxies—the majority of the control galaxies are likely non-void galaxies. However, without further verification, we simply consider these to be “field” galaxies (as none of them appear to have nearby massive host galaxies) throughout the remainder of this analysis.

Finally, three dwarf galaxies were added to the sample as potential objects of interest. These include Pisces A and B, which are nearby dwarf galaxies that have been identified at the boundary between voids and higher-density filaments. Their star formation histories have undergone a recent increase, potentially triggered by gas accretion from a denser environment, suggesting that they are in the process of exiting the voids in which they likely formed ([Tollerud et al. 2016](#)). IFU maps of Pisces A and B will help identify how this environmental transition affects the kinematic and chemical properties of these galaxies.

The last galaxy in the sample, denoted “reines65” in this paper, is ID 65 from [Reines et al. \(2020\)](#), who recently reported discoveries of luminous compact radio sources in nearby dwarf galaxies that are consistent with radiation from accreting black holes. Several of these

³ [OIII] λ 4363 is the weakest of the emission lines required to measure “direct” gas-phase metallicities.

sources appear to be located outside their host galaxies’ central regions, and Reines et al. (2020) suggested that these radio sources are evidence for so-called “wandering” (i.e., off-nuclear) black holes. Optical spectroscopy has previously been employed to search for central supermassive black holes in dwarf galaxies (e.g., Reines et al. 2013; Moran et al. 2014; Sartori et al. 2015), but the IFU data here present the first opportunity for investigating optical radiation from an *off-nuclear* black hole candidate in a dwarf galaxy.

Table 1 lists the properties of our final void and control samples.

2.2. Observations and data reduction

IFU data were obtained for the sample over 2.5 nights using KCWI, an optical integral field spectrograph on the Nasmyth platform of the 10 m Keck II telescope (Morrissey et al. 2018). KCWI has multiple configurations; in order to match the typical angular size of the dwarf galaxies in my sample, we used the medium slicer and blue BL grating centered at $\lambda = 4500 \text{ \AA}$. This combination yields a $20'' \times 16.5''$ field of view, nominal spectral resolution of $\sim 2.5 \text{ \AA}$ ($\sigma \sim 71 \text{ km s}^{-1}$) at 4500 \AA , and a usable wavelength range of $3500 - 5500 \text{ \AA}$.

Table 2 describes the observations of each galaxy. For galaxies with multiple exposures, we rotated the position angles by $\pm 10^\circ$ for each exposure in order to minimize spatial covariance during stacking. For each object exposure, we observed a patch of nearby sky with the same exposure time and position angle to perform sky subtraction. We processed all object exposures using the IDL version of the KCWI data reduction pipeline⁴, which produces flux-calibrated data cubes. Data cubes of the same object were then aligned and stacked using a drizzling algorithm as presented in Chen et al. (2021)⁵.

3. ANALYSIS

The final stacked data cubes are then analyzed using a custom pipeline⁶. Although many of the details are tailored for this specific application, the pipeline follows many of the same general steps as other IFS survey analysis pipelines, including the Mapping Nearby Galaxies at Apache Point Observatory Data Analysis Pipeline (MaNGA DAP; Westfall et al. 2019) and Pipe3D (Sánchez et al. 2016).

⁴ <https://github.com/Keck-DataReductionPipelines/KcwiDRP>

⁵ <https://github.com/yuguangchen1/kcwi>

⁶ The full pipeline, along with all custom code used in this paper, is available at <https://github.com/mdlreyes/void-dwarf-analysis>

3.1. Binning and covariance correction

Some initial steps are taken to prepare the data cubes: the cubes are first corrected for Galactic reddening using the $E(B - V)$ color indices measured by Schlafly & Finkbeiner (2011), and the observed wavelength array is divided by $(1 + z)$ to correct for redshift. Each data cube is then spatially binned to increase the continuum signal-to-noise (S/N). The S/N of an individual spaxel is often too low to reliably fit with stellar continuum templates, particularly in low surface brightness regions like galaxy outskirts or faint dwarf galaxies. We therefore increase the S/N by spatially binning spaxels, i.e., averaging multiple adjacent spaxels. To do this, we use *vorbin*, an adaptive spatial binning algorithm that produces Voronoi tessellations (Cappellari & Copin 2003).

We first define the nominal S/N of an individual spaxel, assuming that each spaxel is independent. Because we are primarily interested in measuring information from the stellar continuum in each spaxel, we use the formula for the detrended *continuum* S/N defined by Rosales-Ortega et al. (2012):

$$\left(\frac{S}{N}\right)_c = \frac{\mu_c}{\sigma_c}, \quad (1)$$

where μ_c is the mean of the flux in the continuum band $f(\lambda)_c$, and σ_c is the detrended standard deviation (i.e., the standard deviation in the difference between $f(\lambda)_c$ and a linear fit to $f(\lambda)_c$). We take $f(\lambda)_c$ to be the flux across the continuum range $4750 - 4800 \text{ \AA}$, which lacks strong emission features.

The S/N values from Equation 1 are likely overestimates, since stacking data cubes introduces covariance between adjacent spaxels. To account for this, rather than computing full covariance matrices for each spaxel in every data cube, we use an empirical formula to estimate the ratio between the “true” noise ϵ_{true} and the noise assuming no covariance $\epsilon_{\text{no covar}}$. This ratio, denoted η , is assumed to be a function of the bin size, with the form suggested by Husemann et al. (2013):

$$\eta = \frac{\epsilon_{\text{true}}}{\epsilon_{\text{no covar}}} = \begin{cases} \beta(1 + \alpha \log N) & N \leq N_{\text{thresh}} \\ \beta(1 + \alpha \log N_{\text{thresh}}) & N > N_{\text{thresh}}. \end{cases} \quad (2)$$

Here, N is the number of spaxels in each bin, α describes the strength of the dependence of η on bin size, and β is a normalization factor. Above a threshold bin size N_{thresh} , additional spaxels are assumed to be far enough apart that they do not add any extra covariance, so the ratio η is capped at a constant.

We estimate the free parameters $\{\alpha, \beta, N_{\text{thresh}}\}$ following the procedure of Law et al. (2016) and using the several modules from the CWITools package (O’Sullivan &

Table 1. General properties of void and field dwarf galaxy sample.

ID ^a	RA	Dec	z^b	g^b	Type ^c
	(J2000)	(J2000)			
1180506	09 12 51.73	+31 40 51.48	0.0064	17.17	v
281238	09 45 40.99	+01 37 03.87	0.0064	18.38	v
1904061	08 48 43.52	+22 55 47.60	0.013	17.93	v
821857	10 06 42.44	+51 16 24.23	0.0162	17.49	v
1158932	09 28 44.47	+35 16 41.14	0.0151	17.42	v
866934	09 16 25.07	+43 00 19.30	0.0085	16.66	v
825059	08 13 39.49	+36 42 34.56	0.0130	16.99	v
2502521	09 13 19.89	+12 32 07.32	0.0161	18.11	v
1228631	10 13 58.42	+39 48 01.62	0.007	15.65	v
1876887	08 49 56.66	+25 41 02.61	0.008	16.67	v
1246626	11 30 11.93	+44 27 16.07	0.0172	17.06	v
1142116	08 18 19.70	+24 31 36.94	0.0073	15.56	v
955106	10 16 28.21	+45 19 17.53	0.0055	14.86	v
1063413	11 23 22.03	+45 45 16.34	0.0202	17.37	v
1074435	09 48 00.79	+09 58 15.43	0.0104	16.30	v
1785212	07 50 41.62	+50 57 40.28	0.0187	17.51	v
1280160	11 07 13.71	+06 24 42.38	0.0085	15.88	v
1782069	10 04 38.88	+67 49 22.05	0.0145	16.99	v
1126100	09 34 03.03	+11 00 21.67	0.0085	15.15	v
Pisces A	00 14 46.00	+10 48 47.01	0.0008	17.56	v
Pisces B	01 19 11.70	+11 07 18.22	0.0020	17.43	v
SDSS J0133+1342	01 33 52.56	+13 42 09.39	0.0087	17.92	f
AGC 112504	01 36 40.92	+15 05 12.14	0.0088	17.84	f
UM 240	00 25 07.43	+00 18 45.63	0.0109	17.04	f
SHOC 150	03 04 57.97	+00 57 14.09	0.0121	17.86	f
LEDA 3524	00 58 55.47	+01 00 17.44	0.0179	16.47	f
LEDA 101427	00 24 25.95	+14 04 10.65	0.0142	15.86	f
IC 0225	02 26 28.29	+01 09 37.92	0.0051	14.06	f
reines65	11 36 42.72	+26 43 37.68	0.0333	15.65	f

^aGalaxy ID. For most void galaxies, these are the galaxy index numbers from the KIAS Value Added Galaxy Catalog (Choi et al. 2010). For most field galaxies, these are the galaxy names preferred by NASA/IPAC Extragalactic Database (NED). The galaxy “reines65” is identified as galaxy 65 from (Reines et al. 2020).

^bRedshifts and g -band magnitudes are from SDSS.

^cGalaxy classification as “v” for void dwarf galaxy or “f” for field dwarf galaxy. Pisces A and B are classified as “void” galaxies for our purposes, although they are likely moving into a cosmic filament (see text).

Table 2. Observations of void and field dwarf galaxies.

Object	Exposures (s)	Position angles ($^{\circ}$)	Date (dd-mm-yy)	Airmass
Void dwarf galaxies				
1180506	2 \times 300	167.6, 177.6	29-12-2019	1.03
281238	2 \times 900	139.9, 149.9	28-12-2019	1.25
1904061	3 \times 800	44.1, 54.1, 64.1	28-12-2019	1.01
821857	2 \times 700	97.4, 107.4	28-12-2019	1.17
1158932	2 \times 700	47.7, 57.7	29-12-2019	1.10
866934	2 \times 300	4.4, 14.4	29-12-2019	1.11
825059	1 \times 600, 2 \times 700, 1 \times 940	20.1, 30.1	30-12-2019	1.20
2502521	2 \times 400	18.0, 28.0	28-12-2019	1.19
	2 \times 800	8.0, 18.0	29-12-2019	1.25
1228631	2 \times 600	16.0	22-01-2020	1.06
1876887	2 \times 400	145.7, 175.7	28-12-2019	1.14
1246626	2 \times 800	49.0	22-01-2020	1.10
1142116	2 \times 900	144.3, 154.3	28-12-2019	1.12
955106	1 \times 600	9.0	22-01-2020	1.12
1063413	4 \times 900	167.0, 177.0	22-01-2020	1.26
1074435	1 \times 600, 3 \times 840	103.0, 113.0	22-01-2020	1.28
1785212	2 \times 400	50.0, 60.0	29-12-2019	1.20
	2 \times 850	50.0, 60.0	30-12-2019	1.50
1280160	2 \times 700	145.0	22-01-2020	1.09
1782069	4 \times 750	37.1, 47.1, 57.1	29-12-2019	1.62
1126100	2 \times 300	149.2, 159.2	29-12-2019	1.02
Pisces A	1 \times 600, 2 \times 1200	0.0, 10.0	28-12-2019	1.11
	2 \times 900	0.0, 10.0	30-12-2019	1.35
Pisces B	1 \times 600, 2 \times 1000	140.0, 150.0	30-12-2019	1.02
Field dwarf galaxies				
SDSS J0133+1342	1 \times 500	128.0	22-01-2020	1.11
AGC 112504	2 \times 900	134.1, 144.1	28-12-2019	1.51
UM 240	4 \times 1000	91.0, 101.0	22-01-2020	1.13
SHOC 150	2 \times 600, 2 \times 660	118.0, 128.0	22-01-2020	1.44
LEDA 3524	2 \times 400	147.4, 157.4	28-12-2019	1.55
LEDA 101427	2 \times 400	14.8, 24.8	30-12-2019	1.54
IC 0225	2 \times 900	167, 177	28-12-2019	1.10
reines65	4 \times 600	45.0, 55.0	22-01-2020	1.10

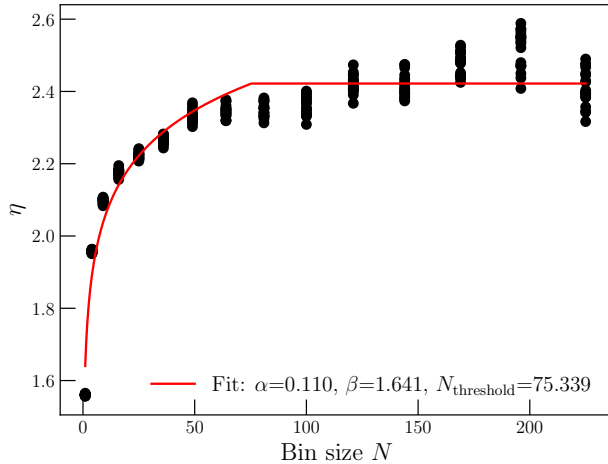


Figure 1. The ratio $\eta = \epsilon_{\text{true}}/\epsilon_{\text{no covar}}$ as a function of bin size for an example with 4 stacked exposures. Black points represent empirical estimates from mock data cubes, as described in the text. The red line indicates the best-fit empirical curve of the form Equation 2.

Chen 2020). First, we create mock data cubes in which all pixels have fluxes independently drawn from a normal distribution $\mathcal{N} \sim (1, 1)$ with mean and variance both unity. These mock cubes are stacked following the same drizzling procedure as the actual data cubes from individual exposures, producing mock intensity and variance cubes. For a stacked cube, the spaxels are binned using a simple boxcar of size n^2 where n varies. The standard deviation of each bin in the mock intensity cube is an estimate of the “true” noise ϵ_{true} , since it accounts for the effects of stacking. The stacked mock variance cube, on the other hand, is used to compute a separate noise estimate $\epsilon_{\text{no covar}}$ using simple error propagation rules, assuming that each spaxel is independent. The ratio of these two estimates can be plotted as a function of bin size N and fit with a curve of the functional form described in Equation 2 to determine the best-fit values of $\{\alpha, \beta, N_{\text{thresh}}\}$. Figure 1 demonstrates an example of this fitting for four stacked exposures, showing that Equation 2 is a good representation of η .

By multiplying this empirical estimate for η by the noise estimate (i.e., dividing Equation 1 by η), the S/N within a bin can be corrected for the effects of spatial covariance. Using covariance-corrected S/N values, the `vorb` algorithm then creates bins with a target S/N while optimally preserving spatial resolution. The target S/N is at least 10 for all galaxies. We attempt to maximize S/N per bin while maintaining spatial resolution; for some galaxies with longer exposures, we set a higher target S/N per bin (for reference, the maximum target S/N is 50 for galaxy 955106).

3.2. Continuum fitting and kinematics measurements

Taking the average spectrum in each bin, we now fit the stellar continuum using the full spectral-fitting algorithm `pPXF` (Cappellari & Emsellem 2004; Cappellari 2017). This algorithm attempts to determine the line-of-sight velocity distribution (LOSVD) of the stars in a galaxy by fitting a galaxy spectrum with a combination of templates. We use templates from the MILES stellar library of single stellar population models (Sánchez-Blázquez et al. 2006; Falcón-Barroso et al. 2011; Vazdekis et al. 2015). These models are produced, assuming a universal Kroupa (2000) stellar initial mass function (IMF), from BaSTI isochrones (Hidalgo et al. 2018), which cover a metallicity range $-2.27 < [\text{Fe}/\text{H}] < +0.40$ and age range 0.03–14.0 Gyr. The spectra in this library have wavelength range 354–741 nm with a constant resolution FWHM of 2.51Å.

The instrumental resolution of KCWI is slightly better, with a FWHM of $\sim 2.4\text{Å}$ (as measured from arc lamps). We correct this for redshift by dividing by $(1+z)$ (see Cappellari 2017), then use a Gaussian kernel to smooth the observed spectra to match the spectral resolution of the templates. Before using the `pPXF` algorithm, we also mask strong gas emission lines from the observed spectra and normalize both observed and template spectra by their median values.

For the i^{th} binned spectrum, `pPXF` recovers the line-of-sight stellar velocity v_i and velocity dispersion $\sigma_{*,i}$. The top two panels of Figure 2 illustrate `pPXF` fits to binned spectra with different S/N. For comparison, the bottom panel shows the integrated (i.e., inverse variance-weighted average) spectrum. `pPXF` is able to fit all spectra despite their varying S/N. Any bins with S/N < 1 (primarily bins that are outside the galaxy) are discarded from the remainder of our analysis. Additionally, velocity dispersion measurements $\sigma_{*,i}$ are also limited by resolution uncertainties: for example, the instrumental dispersion of observed spectra, or mismatches between the resolutions of observed and template spectra (Cappellari 2017). As a result, in some bins `pPXF` may be able to recover accurate stellar velocities but not velocity dispersions. We therefore also discard measurements of $\sigma_{*,i}$ in bins where $\sigma_{*,i} < 1$ km/s, since these are likely to be driven by noise or resolution effects (see, e.g., Sec. 7.4.3 of Westfall et al. 2019). For two galaxies (void galaxies 821857 and 1904061), this criterion leaves < 10 bins (located preferentially near the galaxy centers, which are typically the regions with the lowest $\sigma_{*,i}$); given such a small number of bins, we do not report global velocity dispersions for these galaxies. Finally, we also remove from our analysis two other galaxies (void galaxy

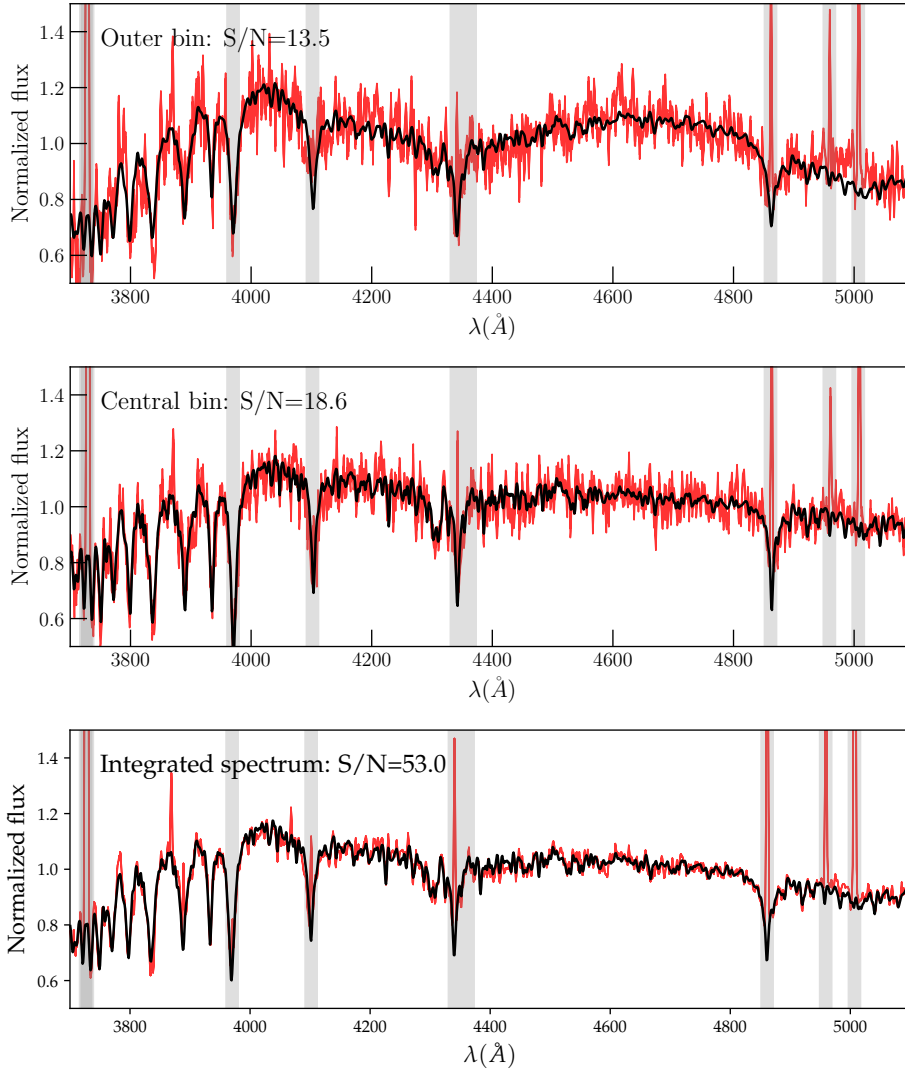


Figure 2. Example pPXF fits for binned and integrated spectra. Top: pPXF fit (black line) to observed spectrum (red line) for a bin in the outer region of field galaxy reines65, with relatively low continuum S/N (Equation 1). Gray shaded regions indicate gas emission lines, which are masked out of the spectrum before fitting. Middle: Same, but for a bin in the center of reines65, with higher S/N. Bottom: Same, but for the integrated spectrum, which has higher S/N than any of the binned spectra.

1074435 and field galaxy SDSS J0133+1342) which had poor wavelength solutions in most of their bins.

We compute the systemic line-of-sight velocity of the galaxy v_{sys} , which we take to be the flux-weighted average of the velocities v_i in each bin. This systematic velocity is subtracted from each of the bin velocities v_i . The resulting maps of stellar (line-of-sight) velocity and velocity dispersion are presented in Figure 3.

These spatially-resolved kinematic maps are then used to compute *global* kinematic estimates. In particular, the global ratio v_{rot}/σ is often used to trace the structural properties of galaxies. Here, v_{rot} is the maximum rotational speed within the galaxy, and σ_* is the intrinsic local velocity dispersion. While models can be used to estimate these global parameters from spatially-

resolved kinematic information, this is unfortunately not a straightforward task for the low-mass dwarf galaxies in our sample. Most of the galaxies in our sample do not have clear velocity gradients and are likely not well-described by simple inclined disk models. More sophisticated models, such as Jeans models, are frequently not well-suited for low-mass galaxies that are not necessarily in dynamical equilibrium (El-Badry et al. 2017).

We therefore consider empirical kinematic statistics. Several recent studies (e.g., Fraser-McKelvie & Cortese 2022) have used the formalism developed by Cappellari et al. (2007) and Binney (2005) for IFU data to estimate v_{rot}/σ_* :

$$\left(\frac{v_{\text{rot}}}{\sigma}\right)^2 = \frac{\sum_i F_i v_i^2}{\sum_i F_i \sigma_{*,i}^2}, \quad (3)$$

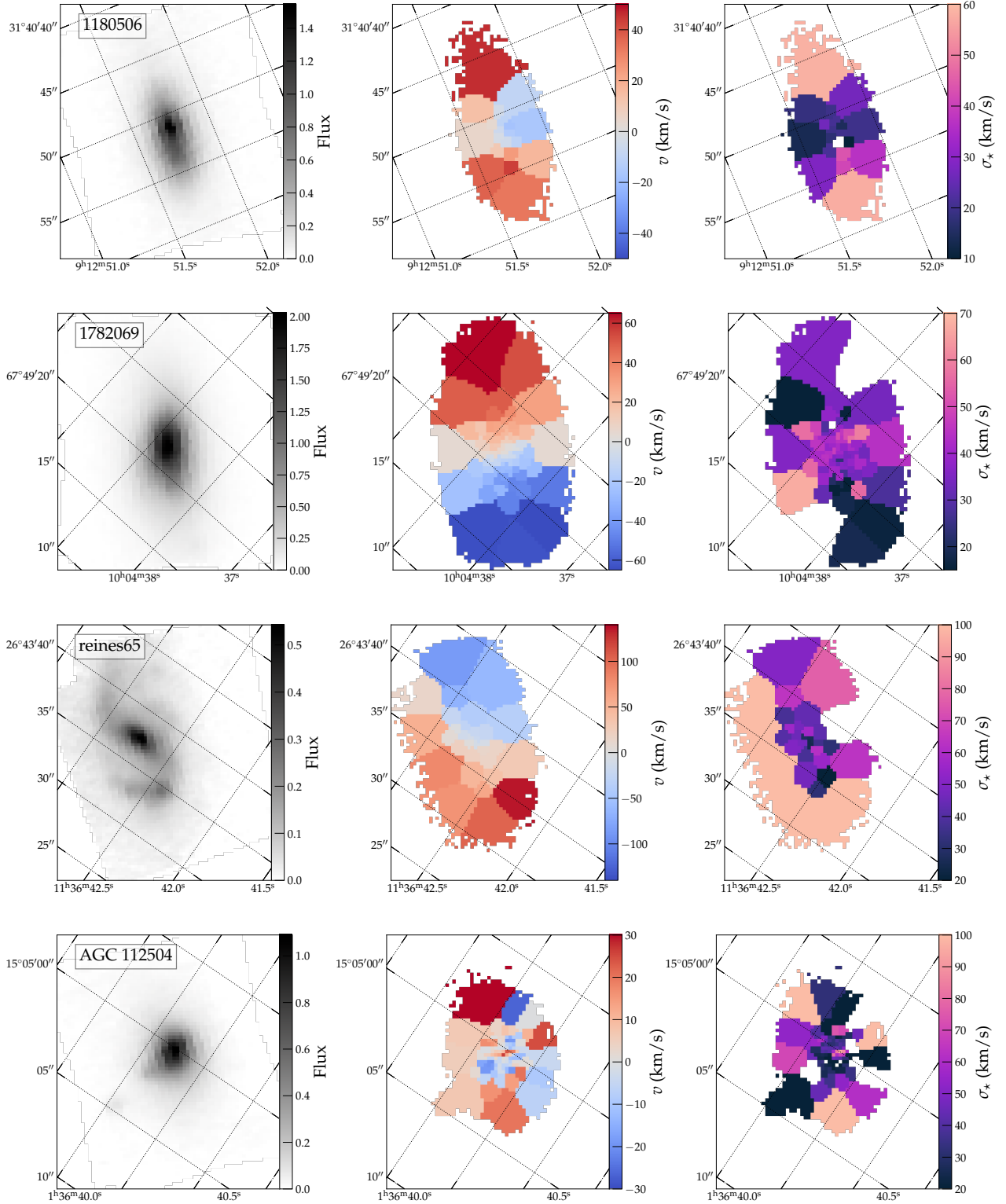


Figure 3. Example stellar kinematic maps of dwarf galaxies. Left: Integrated white-light images (in arbitrary flux units) computed by summing the flux in each IFU spaxel. Center: Maps of line-of-sight stellar velocity v for dwarf galaxies. Right: Maps of line-of-sight stellar velocity dispersion σ_* . As described in the text, bins with $\sigma_{*,i} < 1$ km/s are removed from our calculations, so we do not plot them here. Only some galaxies are presented in this figure; the complete figure set (11 images) is available in the online journal.

where F_i is the total flux in the i^{th} bin. However, Equation 3 was initially developed to measure anisotropy in elliptical galaxies. As [Fraser-McKelvie & Cortese \(2022\)](#) note, brighter central regions are likely to dominate this flux-weighted measurement, leading to lower values of v_{rot}/σ_* —an effect that may be especially problematic for non-elliptical galaxies.

Following a number of IFU studies (e.g., [Law et al. 2009](#)), we instead approximate v_{rot} for a galaxy using the following formula for shear velocity:

$$v_{\text{rot}} = \frac{1}{2}(v_{\text{max}} - v_{\text{min}}). \quad (4)$$

To prevent outliers in v_i from dominating v_{rot} , we define v_{max} and v_{min} as the respective medians of the 95–100th and 0–5th percentiles of v_i in the galaxy’s velocity map ([Herenz et al. 2016](#)). Errors in v_{max} and v_{min} are computed as the ranges of the 95–100th and 0–5th percentile of v_i . Here we take v_i to be the line-of-sight velocity and ignore the geometric effect of inclination angle i ; we discuss the impact of this effect in Section 4.3.3. We then estimate the global stellar velocity dispersion σ_* as the flux-weighted average of the bin velocity dispersions σ_i ([Binney 2005](#)). The final uncertainties in both v_{rot} and σ_* are then computed using standard error propagation. Table 3 summarizes the measured global stellar kinematics (systemic velocities, peak rotational velocities, velocity dispersions, and our final v_{rot}/σ_* estimates) for the dwarf galaxies in the sample.

4. DISCUSSION

The global value of v_{rot}/σ_* is a probe of the stellar motions within a galaxy (e.g., [Illingworth 1977](#); [Bender et al. 1993](#); [Binney 2005](#); [Ferré-Mateu et al. 2021](#)). Higher values of this ratio ($v_{\text{rot}}/\sigma_* \gg 1$) indicate dynamically cold, rotation-supported “disky” systems, while “puffy” dispersion-supported systems like dSphs typically have $v_{\text{rot}}/\sigma_* < 1$. The dependence of v_{rot}/σ_* on external galaxy environment and on intrinsic galaxy properties is therefore a useful metric for understanding the processes that drive galaxy formation and dynamical evolution.

As shown in Table 3, there is no significant difference in v_{rot}/σ_* between the void and field subsamples: on average, the void dwarf galaxies have $\langle v_{\text{rot}}/\sigma_* \rangle = 0.90^{+0.09}_{-0.09}$, while the “control” field galaxies have $\langle v_{\text{rot}}/\sigma_* \rangle = 0.90^{+0.12}_{-0.12}$. The similarity between the galaxies selected to be in voids and the randomly selected “field” galaxies suggests that the large-scale void environment does not significantly affect the stellar kinematics of dwarf galaxies.

In both subsamples, most of the dwarf galaxies (12/20 void dwarf galaxies and 6/7 field dwarf galaxies) are pri-

marily dispersion-supported, with $v_{\text{rot}}/\sigma_* < 1$. All have $v_{\text{rot}}/\sigma_* < 2$, implying that none of them is strongly rotating. Both subsamples have slightly higher v_{rot}/σ_* than Local Group dwarf galaxies on average ($\langle v_{\text{rot}}/\sigma_* \rangle = 0.50^{+0.09}_{-0.09}$; [Wheeler et al. 2017](#)). In the following sections, we discuss potential physical implications for this discrepancy.

4.1. Disk formation as a function of proximity to a massive galaxy

We now consider the effect of local environment on dwarf galaxy kinematics. In particular, our v_{rot}/σ_* measurements allow us to directly test the predictions of the tidal stirring model. In this model, which posits that tidal interactions remove angular momentum from dwarf galaxy disks during pericentric passages, v_{rot}/σ_* is expected to increase with increasing distance from a massive galaxy ([Kazantzidis et al. 2011](#)). [Wheeler et al. \(2017\)](#) did a systematic search of 40 Local Group dwarf galaxies and did not find evidence of a trend between v_{rot}/σ_* and distance d_{L^*} to a massive host (i.e., the Milky Way or M31). Since void dwarf galaxies are typically extremely isolated, they can be used to extend this analysis to higher d_{L^*} .

We first use the SDSS DR17 catalog to locate the closest massive neighbor to each dwarf galaxy in our sample. We identify all galaxies with apparent magnitudes $14 < g < 20$ mag and compute their stellar masses using mid-infrared photometry measured from the Wide-field Infrared Survey Explorer (WISE; [Wright et al. 2010](#)). We use the empirical relation from [Cluver et al. \(2014\)](#) for resolved low-redshift sources:

$$\log_{10} M_*/L_{W1} = -2.54(W_{3.4 \mu\text{m}} - W_{4.6 \mu\text{m}}) - 0.17, \quad (5)$$

where $L_{W1}(L_{\odot}) = 10^{-0.4(M_{W1} - 3.24)}$. Here, M_{W1} is the absolute magnitude of the source in the WISE 3.4 μm band and $W_{3.4 \mu\text{m}} - W_{4.6 \mu\text{m}}$ is the rest-frame color. These magnitudes and colors are obtained from the WISE “forced photometry” catalog produced for SDSS ([Lang et al. 2016](#)). For each of the dwarf galaxies in our sample, we then compute three-dimensional distances to all massive ($M_* > 10^{10} M_{\odot}$) neighbors, using SDSS coordinates and spectroscopic redshifts⁷ and identify the nearest massive neighbor. The distances to the nearest massive galaxies, d_{L^*} , are listed in Table 3.

As expected, the void dwarf galaxies in our sample are extremely isolated, with $d_{L^*} \gtrsim 1$ Mpc. Interestingly, most of the randomly selected field galaxies also

⁷ To convert redshifts to distances, we assume a flat Λ CDM cosmology with Planck 2018 parameters ($H_0 = 67.4 \text{ km s}^{-1} \text{ Mpc}^{-1}$, $\Omega_m = 0.315$; [Aghanim et al. 2020](#)).

Table 3. Stellar kinematics and derived properties of void and field dwarf galaxies.

Object	v_{sys} (km/s)	v_{rot} (km/s)	σ_* (km/s)	v_{rot}/σ_*	d_{L*} (kpc)	$\log M_{\star}^a$ [M_{\odot}]	i ($^{\circ}$)
Void dwarf galaxies							
1180506	35.36	30.75 ± 1.47	23.10 ± 2.96	1.33 ± 0.18	3070.1	$7.55^{+0.23}_{-0.23}$	65.5
281238	85.26	39.88 ± 13.24	54.98 ± 12.14	0.73 ± 0.29	5284.1	$6.88^{+0.38}_{-0.38}$	58.3
1904061 ^b	67.02	22.95 ± 4.44	3181.9	$6.91^{+0.35}_{-0.36}$	20.3
821857 ^b	89.80	50.08 ± 20.01	5960.8	$7.49^{+0.30}_{-0.30}$	59.4
1158932	45.07	22.29 ± 7.26	39.62 ± 12.30	0.56 ± 0.25	3033.7	$7.65^{+0.37}_{-0.36}$	69.0
866934	74.27	38.37 ± 13.96	33.68 ± 5.02	1.14 ± 0.45	1955.5	$8.36^{+0.20}_{-0.20}$	68.6
825059	83.29	22.60 ± 8.23	32.08 ± 3.15	0.70 ± 0.27	2769.9	$8.14^{+0.34}_{-0.35}$	63.1
2502521	64.56	40.14 ± 9.89	38.60 ± 10.40	1.04 ± 0.38	1542.5	$9.53^{+0.57}_{-0.58}$	62.7
1228631	55.78	26.57 ± 5.31	46.95 ± 4.11	0.57 ± 0.12	3036.6	$7.87^{+0.13}_{-0.14}$	57.3
1876887	94.82	35.58 ± 13.36	23.58 ± 6.03	1.51 ± 0.69	3486.5	$8.21^{+0.17}_{-0.17}$	57.7
1246626	51.66	58.13 ± 20.68	70.15 ± 19.78	0.83 ± 0.38	5862.8	$7.63^{+0.25}_{-0.26}$	58.5
1142116	123.18	18.59 ± 7.27	56.24 ± 1.32	0.33 ± 0.13	8132.2	$8.58^{+0.14}_{-0.13}$	47.2
955106	90.30	16.75 ± 2.42	22.36 ± 4.55	0.75 ± 0.19	4416.1	$8.64^{+0.09}_{-0.09}$	45.1
1063413	18.10	52.65 ± 18.34	29.65 ± 3.33	1.78 ± 0.65	4795.5	$8.66^{+0.21}_{-0.21}$	74.6
1074435 ^c
1785212	71.42	38.66 ± 17.93	21.50 ± 5.47	1.80 ± 0.95	2238.2	$8.78^{+0.17}_{-0.17}$	44.0
1280160	73.56	14.65 ± 3.88	34.61 ± 1.48	0.42 ± 0.11	2449.1	$8.59^{+0.17}_{-0.17}$	48.1
1782069	70.05	58.95 ± 16.46	38.51 ± 2.20	1.53 ± 0.44	2440.1	$8.82^{+0.11}_{-0.11}$	61.2
1126100	-11.55	42.86 ± 5.54	34.92 ± 1.20	1.23 ± 0.16	847.4	$9.32^{+0.09}_{-0.09}$	38.6
PiscesA	98.44	65.24 ± 23.37	139.19 ± 16.46	0.47 ± 0.18	4265.5
PiscesB	120.78	28.48 ± 1.36	144.35 ± 48.10	0.20 ± 0.07	1760.8
Field dwarf galaxies							
SDSS J0133+1342 ^c
AGC 112504	115.55	25.81 ± 8.74	39.22 ± 5.22	0.66 ± 0.24	7071.5	$7.89^{+0.28}_{-0.29}$	36.7
UM 240	-130.73	20.26 ± 3.31	39.31 ± 10.98	0.52 ± 0.17	10227.2	$7.48^{+0.33}_{-0.33}$	43.0
SHOC 150	106.69	22.38 ± 1.14	23.06 ± 5.45	0.97 ± 0.23	3948.7	$7.20^{+0.20}_{-0.20}$	57.8
LEDA 3524	101.15	32.44 ± 2.50	35.08 ± 8.28	0.92 ± 0.23	1235.3	$7.65^{+0.25}_{-0.26}$	66.1
LEDA 101427	109.00	16.74 ± 6.16	18.53 ± 3.75	0.90 ± 0.38	4287.5	$8.62^{+0.19}_{-0.18}$	58.6
IC 0225	123.46	20.22 ± 8.11	31.87 ± 2.66	0.63 ± 0.26	1700.8	$8.55^{+0.10}_{-0.10}$	30.2
reines65	127.08	93.65 ± 24.93	58.37 ± 9.50	1.60 ± 0.50	545.4	$7.51^{+0.24}_{-0.25}$	57.0

^aStellar masses are calculated as described in Section 4.2.

^bAs described in the text, we did not compute σ_* for these galaxies because they had < 10 bins in which the velocity dispersion is large enough to be a reliable measurement.

^cAs described in the text, the wavelength solutions for these galaxies are poor, so we do not consider their kinematic measurements in the rest of this paper.

appear to have similarly high values of d_{L^*} . This is not entirely surprising: as discussed in Section 2.1, the field dwarf galaxies could not be directly compared against the void catalogs used to select the void galaxies, and some of them may in fact be located in large-scale void environments. Furthermore, we emphasize that d_{L^*} is a measure of *local* isolation that may not necessarily correspond with large-scale (i.e., void-scale) environment; while void galaxies are expected to have high d_{L^*} , galaxies with high d_{L^*} may not necessarily be in voids.

The top panel of Figure 4 plots v_{rot}/σ_* as a function of d_{L^*} . The void and field dwarf galaxies in our sample are plotted as purple empty and filled circles, respectively, while Wheeler et al. (2017)’s measurements of Local Group satellite (dSph) and isolated (dIrr) galaxies are respectively plotted as orange filled and empty squares. A small number of ultra-faint dwarf galaxies, also measured by Wheeler et al. (2017), are shown as filled green triangles for comparison.

The void and field dwarf galaxies in our sample have higher d_{L^*} than most of the Local Group galaxies, and they are located well outside the virial radii of any massive halos (for the Milky Way and M31, $R_{\text{vir}} \sim 300$ kpc). Some studies have shown that dark matter halos can produce environmental effects at even greater radii—for example, so-called “backsplash” dwarf galaxies may have been within the virial radius of a host galaxy at earlier times in their orbits, despite currently being located outside R_{vir} (e.g., Buck et al. 2019, and references therein). Almost all the dwarf galaxies in our sample are located far enough from massive galaxies that they are unlikely to be backsplash galaxies (see, e.g., More et al. 2015, who predict a “splashback” radius of $\sim 2.5R_{\text{vir}}$, or ~ 750 kpc for Milky Way-like galaxies).

Additionally, in tidal stirring models, dIrrs require > 10 Gyr of repeated pericentric passages within a massive host’s gravitational potential to complete the full conversion to dSphs (e.g., Table 3 of Kazantzidis et al. 2017). In order to have had such prolonged tidal interactions in the past, many of the dwarf galaxies in our sample would have had to move extremely far from their massive hosts in a short time. For a galaxy with $d_{L^*} \sim 3000$ kpc to have left its host within the last 3 Gyr, it would have needed to move away from its host with an average speed of ~ 1000 km s $^{-1}$; for comparison, the LMC and SMC are estimated to be infalling on the Milky Way with velocities on the order of ~ 300 km s $^{-1}$ (Kallivayalil et al. 2013). We therefore expect our sample to consist of dwarf galaxies that have not been affected by environmental processes like tidal stirring.

Assuming our sample does represent truly isolated dwarf galaxies, the relatively low values of $v_{\text{rot}}/\sigma_* < 2$

that we measure are consistent with the results of some analytic calculations (Kaufmann et al. 2007) and hydrodynamic simulations (Wheeler et al. 2017; Frings et al. 2017), which find that isolated dwarf galaxies naturally form as dispersion-supported systems. However, our measurements are at odds with previous studies of tidal stirring, which typically assume that isolated dwarf galaxies are rotationally supported disks with $v_{\text{rot}}/\sigma_* \approx 2$ (Kazantzidis et al. (2017)). Furthermore, as shown in the top panel of Figure 4, there is no strong trend between v_{rot}/σ_* and d_{L^*} , as would be expected from tidal stirring models. We conclude that tidal interactions are not needed to produce dispersion-supported dwarf galaxies.

4.2. Disk formation as a function of stellar mass

If, as our measurements suggest, low-mass galaxies are dispersion-supported stellar systems even in extreme isolation, perhaps they in fact form as “puffy” systems rather than disks. Indeed, isolated dwarf galaxies in zoom-in hydrodynamic simulations appear to have low stellar v_{rot}/σ_* without being subjected to external perturbations (Wheeler et al. 2017). Yet dynamically cold disks are common among more massive galaxies, perhaps implying that there is a critical stellar mass required to form a disk. Some studies have estimated such a critical mass using morphological observations; for example, Sánchez-Janssen et al. (2010) find that galaxies below $M_* = 2 \times 10^9 M_\odot$ appear substantially thicker in terms of observed axial ratios b/a . We now aim to expand on this work by using stellar kinematics, rather than morphological criteria, to search for a transition between dispersion-supported dwarfs and rotation-dominated massive galaxies.

We compute stellar masses for our galaxies using WISE photometry, following Equation 5. The mid-infrared magnitudes are obtained directly from the WISE All-Sky Data Release Source Catalog (Cutri & et al. 2012); we find that using the Lang et al. (2016) “forced photometry” SDSS catalog, as we did for the massive neighbor galaxies, does not significantly affect our results. Table 3 lists the stellar masses for our sample. We consider the effect of different stellar mass calibrations in Section 4.3.2.

The bottom panel of Figure 4 illustrates the relation between v_{rot}/σ_* and stellar mass. Wheeler et al. (2017) found no clear trend between v_{rot}/σ_* and M_* for Local Group dwarf galaxies across the mass range $M_* = 10^{3.5} - 10^8 M_\odot$. Our sample (purple circles) extends this relation to higher masses. We see a slight upward trend in v_{rot}/σ_* , particularly above $M_* \sim 10^7 M_\odot$. To quantify this trend, we use simple linear regression,

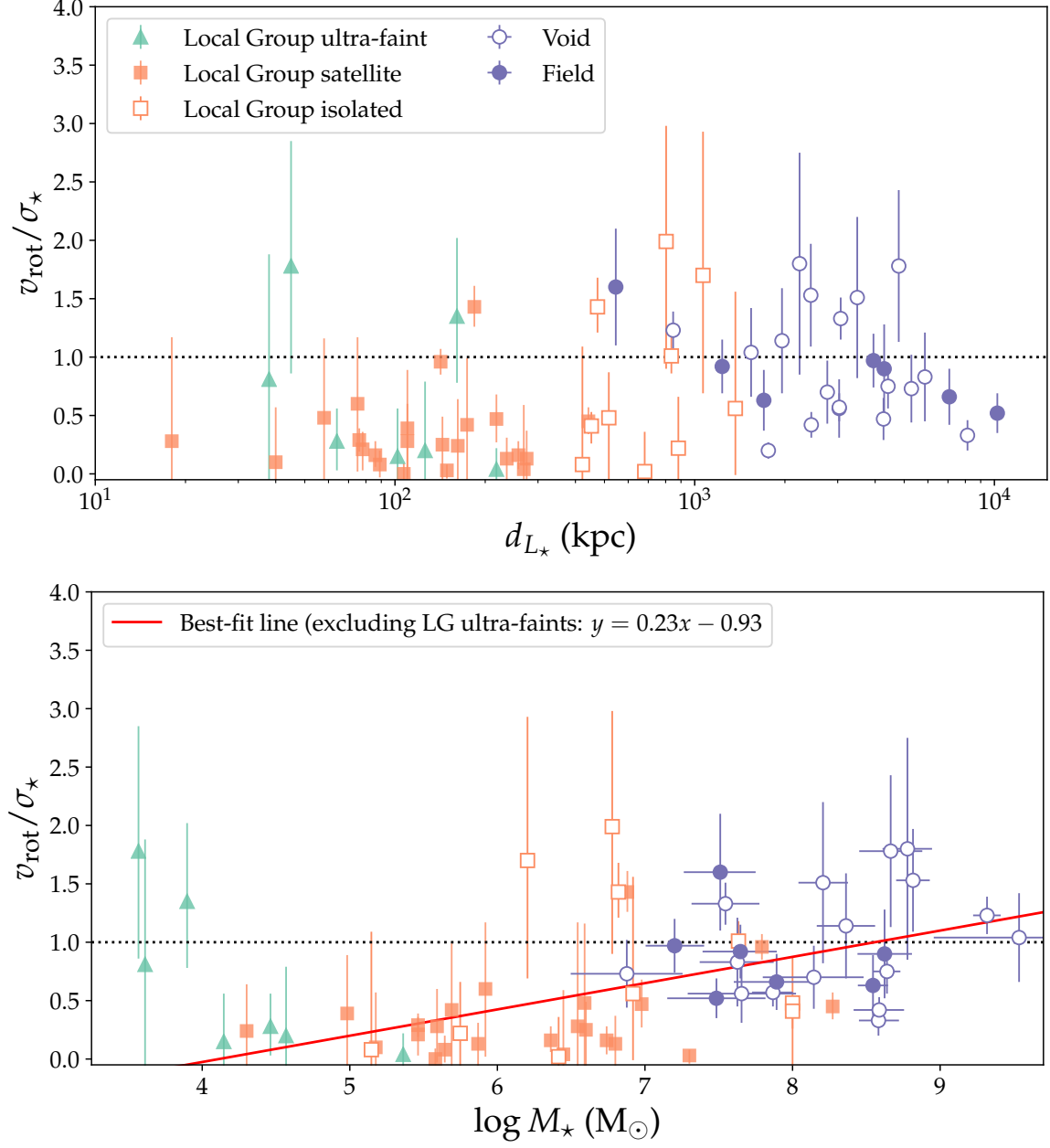


Figure 4. Stellar rotation support (v_{rot}/σ_*) as a function of distance from closest massive galaxy d_{L_*} (top) and stellar mass (bottom). Measurements for Local Group galaxies—ultra-faint dwarf galaxies (green triangles), MW and M31 satellites (filled orange squares), and isolated dwarf galaxies (open orange squares)—are taken from the compilation of Wheeler et al. (2017). Measurements from this work are denoted as purple circles: filled circles denote “field” galaxies from the control sample, while open circles denote void galaxies.

which yields the best-fit line

$$v_{\text{rot}}/\sigma_* = 0.23^{+0.05}_{-0.05}(\log M_*/M_\odot) - 0.93^{+0.37}_{-0.38}. \quad (6)$$

We exclude the ultra-faint dwarf galaxies from this fit, since their relatively high v_{rot} are likely the result of tidal distortion rather than coherent rotation (Simon & Geha 2007).

Despite this upward trend, it is evident that the low-mass galaxies plotted in Figure 4 are kinematically dis-

tinct from the thin disks seen in high-mass galaxies (for comparison, the Milky Way has $v_{\text{rot}}/\sigma_* \sim 20$). Measurements of stellar v_{rot}/σ_* at higher stellar masses ($M_* \gtrsim 10^9 M_\odot$) are needed to identify whether the transition between dispersion-supported dwarfs and rotation-dominated massive galaxies is a gradual trend or a sharp discontinuity.

4.3. Limitations of this study

We now consider potential limitations of this study, including sources of errors that may affect our results.

4.3.1. Selection effects

Our sample is not mass complete, and our selection may bias our results. As described in Section 2.1, we preferentially select dwarf galaxies with high [OIII] λ 4363 fluxes. This would bias our sample towards galaxies with lower gas-phase metallicities at a given stellar mass. At a given stellar mass, gas-phase metallicity may be inversely correlated with specific star formation rate (the “fundamental metallicity relation”; see, e.g., Section 5.2 of [Maiolino & Mannucci 2019](#), and references therein), which may in turn be inversely correlated with velocity dispersion (e.g., [Wake et al. 2012](#); [van der Wel et al. 2016](#), although note that these studies have focused on *gas* kinematics in galaxies more massive ($> 10^9 M_\odot$) than our sample).

Assuming these correlations hold for our sample, the dwarf galaxies in our sample may therefore be biased toward lower velocity dispersions—and higher v_{rot}/σ_* —at a given stellar mass. In other words, a more representative sample of dwarf galaxies at similar masses might have *lower* average v_{rot}/σ_* values than our sample. This further strengthens our main finding that isolated dwarf galaxies are dispersion-supported systems with low v_{rot}/σ_* . This would also decrease the discrepancy between Local Group dwarf galaxies and isolated dwarf galaxies and weaken the trend between v_{rot}/σ_* and M_* , although the potential magnitude of this effect is difficult to estimate.

4.3.2. Uncertainties in secondary parameters

There are a number of systematic effects that may impact our measurements of the galaxy properties d_{L^*} and M_* . First, our d_{L^*} estimates rely on SDSS redshifts. Not only is there intrinsic scatter in the Hubble relation, but SDSS spectroscopic redshifts also have an uncertainty of $\Delta(cz) \sim 30$ km/s ([Abazajian et al. 2005](#)). Combined, these can correspond to distance uncertainties of up to thousands of kpc. We test the effect of these uncertainties by randomly perturbing our d_{L^*} measurements (assuming a normal distribution with a standard deviation 1000 kpc). We find that our main qualitative result—that there is no strong trend between v_{rot}/σ_* and d_{L^*} —does not change.

The stellar masses are also uncertain. In Section 4.2 we chose to compute masses using available mid-infrared photometry from WISE, which is ideal for tracing old stellar populations that may be outshone by younger stars in the optical ([Jarrett et al. 2013](#)). We now compare these WISE masses with optical-based stellar mass

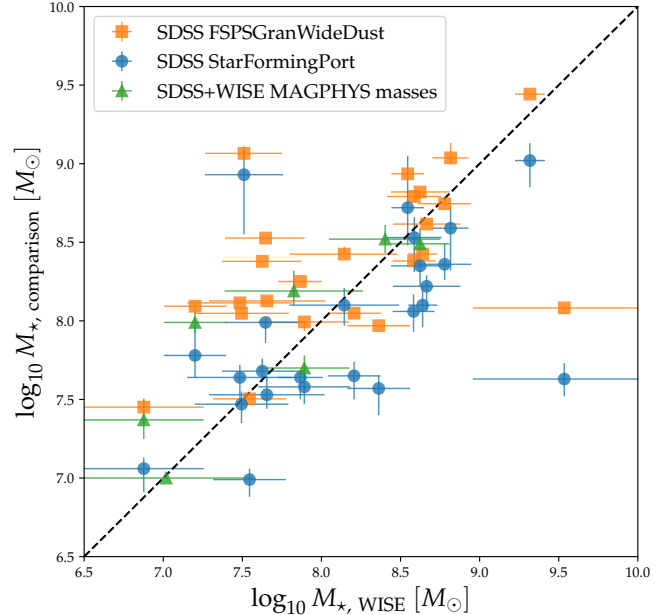


Figure 5. Comparison between stellar masses measured from WISE (x -axis) and stellar masses measured from other calibrations (y -axis). These include the Portsmouth calibration (blue circles; [Maraston 2005](#)), the Granada calibration (orange squares; [Conroy et al. 2009](#)), and the SDSS+WISE MAGPHYS catalog (green triangles; [Chang et al. 2015](#)).

calibrations in Figure 5. We first consider two stellar mass estimates that are available as SDSS value-added catalogs. The star-forming Portsmouth method (“Star-FormingPort,” blue circles) fits SDSS photometry with a stellar evolution model comprised of a metallicity and one of three star-formation histories ([Maraston 2005](#)). The Granada method (“FSPSGranWideDust,” orange squares) uses the Flexible Stellar Population Synthesis models of [Conroy et al. \(2009\)](#) to fit SDSS photometry; we use the WideDust version, which allows for extended star formation histories and accounts for dust extinction. Finally, we obtain stellar masses from [Chang et al. \(2015\)](#), who use the MAGPHYS algorithm to fit combined SDSS+WISE photometry.⁸

We find significant scatter between the different stellar mass estimates, reflecting the many assumptions inherent in modeling galaxy spectral energy distributions ([Conroy 2013](#)). The Portsmouth method yields stellar masses that are systematically lower than the WISE masses (rms deviation of ~ 0.6 dex), while the Granada method yields stellar masses that are systematically higher than the WISE masses (with similar rms

⁸ Although we searched other catalogs, including the GALEX-SDSS-WISE Legacy Catalog ([Salim et al. 2016](#)), we did not find any overlap between these catalogs and our sample.

deviation of ~ 0.6 dex). Only a small number of galaxies in our sample have M_* measurements in the MAGPHYS catalog, so it is difficult to make quantitative comparisons. However, in Figure 5 the MAGPHYS masses are qualitatively more consistent with the WISE masses than the other SDSS calibrations are—perhaps not surprising, since the MAGPHYS catalog uses WISE data. Regardless of overall agreement (or lack thereof) between these stellar mass calibrations, we find that using different calibrations does not impact our results; in particular, the best-fit trend in Equation 6 does not change within parameter uncertainties.

4.3.3. Uncertainties in v_{rot}/σ_*

While our qualitative conclusions are not significantly affected by systematic uncertainties on the x -axes of Figure 4, additional systematic effects may result from our choice of kinematic statistic on the y -axis. As we have defined them, v_{rot} and σ_* are not perfect tracers of stellar rotation and dispersion.

For example, if a galaxy’s angular momentum vector is inclined relative to the line-of-sight by angle i , then the line-of-sight v_{rot} we measure is a lower limit to the intrinsic velocity: $v_{\text{rot}} = v_{\text{rot}}^{\text{intrinsic}} \sin i$. We can correct for this effect by estimating inclination angles i from photometric axis ratios: $i = \cos^{-1}(b/a)$, where a and b are the semi-major and semi-minor axes measured by SDSS r -band exponential model fits. We report i in Table 3 for completeness.

Applying these first-order inclination corrections to our sample increases v_{rot}/σ_* for all galaxies in our sample. Three galaxies become more strongly disk-like (i.e., consistent with $v_{\text{rot}}^{\text{intrinsic}}/\sigma_* \gtrsim 2$): the v_{rot}/σ_* for void galaxy 1785212 changes from 1.80 to 2.59, for void galaxy 1126100 from 1.23 to 1.97, and for field galaxy reines65 from 1.60 to 1.91. These corrections also slightly increase the overall discrepancy between $v_{\text{rot}}^{\text{intrinsic}}/\sigma_*$ of Local Group dwarf galaxies and our isolated dwarf galaxies. The correlation between v_{rot}/σ_* and M_* , for example, becomes stronger:

$$v_{\text{rot}}/\sigma_* = 0.31_{-0.05}^{+0.05} (\log M_*/M_\odot) - 1.43_{-0.38}^{+0.38}. \quad (7)$$

On the other hand, many of our conclusions do not change even after correcting for inclination. The void and field subsamples still have similar $v_{\text{rot}}^{\text{intrinsic}}/\sigma_*$ values. Several of the galaxies in our sample still have relatively low $v_{\text{rot}}^{\text{intrinsic}}/\sigma_* < 1$, and most remain below $v_{\text{rot}}^{\text{intrinsic}}/\sigma_* \sim 2$, which is the value frequently used as an initial condition in tidal stirring simulations. We continue to conclude that environmental effects are not required to produce “puffy” stellar systems. Finally, the corrections described above may not be appropriate for

galaxies that are not inclined disks—and as the line-of-sight velocity maps make clear, most dwarf galaxies in our sample have irregular morphologies and do not display signs of any coherent velocity structure that would be expected in a disk.

Another intrinsic limitation of our kinematic measurements is that although they are derived from spatially resolved IFU data, they are not actually measurements of resolved stars. Comparisons with measurements of galaxies in the Local Group—which *have* been derived from individual stellar velocities—are therefore not direct “apples-to-apples” comparisons. Some studies have begun bridging this gap in recent years by comparing resolved stellar measurements with IFU or integrated-light measurements for individual dwarf galaxies. For example, Ruiz-Lara et al. (2018) obtained both resolved stellar photometry and an integrated-light long-slit spectrum for Local Group dwarf galaxy Leo A and found that both measurement techniques yielded consistent star formation histories. Similarly, Zhuang et al. (2021) found that stellar metallicity estimates from integrated light were consistent with measurements from resolved stellar spectroscopy for M31 satellite NGC 147. To our knowledge such a comparison for stellar kinematics measurements has not yet been done in one galaxy—let alone a systematic analysis of a population of galaxies. In light of these observational obstacles, simulations may be the most promising tool to address this question, since they could be used to produce mock observations in order to quantify systematic differences between resolved and IFU observations.

5. CONCLUSIONS

Using the Keck Cosmic Web Imager, we have obtained IFU spectroscopy for a number of dwarf galaxies ($M_* = 10^7 - 10^9 M_\odot$) located inside and outside of cosmic voids. In this work, we investigated the stellar dynamics of these galaxies by measuring their spatially resolved stellar velocities and stellar velocity dispersions. From these spatially resolved measurements, we estimated global values of v_{rot}/σ_* , a parameter that probes the ratio of stellar rotation to dispersion. Our findings are as follows.

1. We find no significant difference between v_{rot}/σ_* for the dwarf galaxies in cosmic voids and the “field” dwarf galaxies, suggesting that isolated dwarf galaxies have similar stellar dynamics regardless of large-scale environment.
2. Environmental processes in general do not appear to be primary drivers of the dynamical formation of field dwarf galaxies. The majority

of dwarf galaxies in our sample are, like Local Group dwarf galaxies, predominantly dispersion-supported ($v_{\text{rot}}/\sigma_{\star} \lesssim 1$), and we find no correlation between $v_{\text{rot}}/\sigma_{\star}$ and distance to the closest massive galaxy $d_{L^{\star}}$. This confirms the results of Wheeler et al. (2017), who find a similar lack of trend among Local Group dwarf galaxies. These results are further evidence that dSphs/dEs form as “puffy” dispersion-supported systems, rather than as rotation-supported disks that are converted by tidal interactions into dispersion-supported spheroidal systems (the “tidal stirring” hypothesis).

3. We find evidence that $v_{\text{rot}}/\sigma_{\star}$ begins to increase with galaxy stellar mass at $M_{\star} \gtrsim 10^7 M_{\odot}$. However, measurements at higher M_{\star} are needed to identify the transition to strongly rotation-dominated ($v_{\text{rot}}/\sigma_{\star} \gg 2$) disks in higher-mass galaxies.
4. We consider a number of limitations of our study, including uncertainties on $d_{L^{\star}}$, M_{\star} , and $v_{\text{rot}}/\sigma_{\star}$. We find that while known uncertainties in $d_{L^{\star}}$ and M_{\star} are unlikely to impact our results, $v_{\text{rot}}/\sigma_{\star}$ may be subject to a number of systematic effects that could modify some of our conclusions (for example, inclination effects may strengthen a correlation between $v_{\text{rot}}/\sigma_{\star}$ and M_{\star}). Yet even accounting for these effects, many of the galaxies in our sample still have $v_{\text{rot}}/\sigma_{\star} < 2$. Our most conservative conclusion is therefore that environmental effects are not strictly required to make dispersion-supported, low-mass galaxies.

Further investigation is needed to understand other potential systematic effects, particularly the effect of spatial resolution. In other words, are stellar kinematic measurements obtained from resolved stellar populations (as for Local Group dwarf galaxies) systematically different from stellar kinematic measurements obtained from IFU data (as this paper does)? This question also represents a broader issue for the astrophysical community: the Local Group has long served as a benchmark for theories of low-mass galaxy formation and evolution, yet the methods we use to observe Local Group galaxies are very different from those used to study more dis-

tant galaxies. As we begin to explore statistical populations of low-mass galaxies beyond the Local Group, it is critical to understand how differences in observational techniques can impact our measurements. Future simulations and observations can provide a path forward.

In the meantime, integral field spectroscopy remains one of our most promising tools for obtaining spatially resolved observations of low-mass galaxies beyond the Local Group. As this study demonstrates, dwarf galaxies located in cosmic voids are a particularly interesting sample for targeting with IFU surveys, since they can probe in-situ physical processes by minimizing the effect of environment. Measuring stellar kinematics is just one of the many applications of the KCWI dataset presented in this study. In future work, we will investigate other properties that are observable from these rich data; in particular, ionized gas kinematics will provide a useful comparison to the stellar kinematics presented here.

This material is based upon work supported by the National Science Foundation under grant No. AST-2233781. MADLR acknowledges the financial support of the NSF Graduate Research Fellowship and the Stanford Science Fellowship. ZZ acknowledges the financial support of the NASA FINESST Program (No. 80NSSC22K1755). CCS has been supported in part by NSF AST-2009278.

This research has made use of NASA’s Astrophysics Data System Bibliographic Services.

There are many communities without whom this work would not have been possible. We acknowledge that this work is rooted in Western scientific practices and is the material product of a long and complex history of settler-colonialism. MADLR and ENK wish to recognize their status as settlers on the ancestral lands of the Muwekma Ohlone Tribe and the Potawatomi people, and to recognize that the astronomical observations described in this paper were only possible because of the dispossession of Maunakea from Kānaka Maoli. We hope to work toward a scientific practice guided by pono and a future in which we all honor the land.

Facilities: Keck:II (KCWI)

Software: Matplotlib (Hunter 2007), Astropy (Robitaille et al. 2013), Scipy (Jones et al. 2001–), CWITools (O’Sullivan & Chen 2020)

REFERENCES

- Abazajian, K., Adelman-McCarthy, J. K., Agüeros, M. A., et al. 2005, *AJ*, 129, 1755.
<https://doi.org/10.1086/427544>
- Abazajian, K. N., Adelman-McCarthy, J. K., Agüeros, M. A., et al. 2009, *ApJS*, 182, 543.
<https://doi.org/10.1088/0067-0049/182/2/543>

- Aghanim, N., Akrami, Y., Ashdown, M., et al. 2020, *A&A*, 641, A6. <https://doi.org/10.1051/0004-6361/201833910>
- Ahumada, R., Prieto, C. A., Almeida, A., et al. 2020, *ApJS*, 249, 3. <https://doi.org/10.3847/1538-4365/ab929e>
- Bender, R., Burstein, D., & Faber, S. M. 1993, *ApJ*, 411, 153. <https://doi.org/10.1086/172815>
- Beygu, B., Kreckel, K., van der Hulst, J. M., et al. 2016, *MNRAS*, 458, 394. <https://doi.org/10.1093/mnras/stw280>
- Beygu, B., Peletier, R. F., van der Hulst, J. M., et al. 2017, *MNRAS*, 464, 666. <https://doi.org/10.1093/mnras/stw2362>
- Binney, J. 2005, *MNRAS*, 363, 937. <https://doi.org/10.1111/j.1365-2966.2005.09495.x>
- Bond, J. R., Kofman, L., & Pogosyan, D. 1996, *Nature*, 380, 603. <https://doi.org/10.1038/380603a0>
- Buck, T., Macciò, A. V., Dutton, A. A., Obreja, A., & Frings, J. 2019, *MNRAS*, 483, 1314. <https://10.1093/mnras/sty2913>
- Cappellari, M. 2017, *MNRAS*, 466, 798. <https://doi.org/10.1093/mnras/stw3020>
- Cappellari, M., & Copin, Y. 2003, *MNRAS*, 342, 345. <https://doi.org/10.1046/j.1365-8711.2003.06541.x>
- Cappellari, M., & Emsellem, E. 2004, *PASP*, 116, 138. <https://doi.org/10.1086/381875>
- Cappellari, M., Emsellem, E., Bacon, R., et al. 2007, *MNRAS*, 379, 418. <https://doi.org/10.1111/j.1365-2966.2007.11963.x>
- Chang, Y.-Y., van der Wel, A., da Cunha, E., & Rix, H.-W. 2015, *ApJS*, 219, 8. <https://doi.org/10.1088/0067-0049/219/1/8>
- Chen, Y., Steidel, C. C., Erb, D. K., et al. 2021, *MNRAS*, 508, 19. <https://doi.org/10.1093/mnras/stab2383>
- Choi, Y.-Y., Han, D.-H., & Kim, S. S. 2010, *Journal of Korean Astronomical Society*, 43, 191. <https://doi.org/10.5303/JKAS.2010.43.6.191>
- Cluver, M. E., Jarrett, T. H., Hopkins, A. M., et al. 2014, *ApJ*, 782, 90. <https://doi.org/10.1088/0004-637X/782/2/90>
- Conroy, C. 2013, *ARA&A*, 51, 393
- Conroy, C., Gunn, J. E., & White, M. 2009, *ApJ*, 699, 486. <https://doi.org/10.1088/0004-637X/699/1/486>
- Cutri, R. M., & et al. 2012, *VizieR Online Data Catalog*, II/311. <https://ui.adsabs.harvard.edu/abs/2012yCat.2311....0C>
- Desjacques, V., Jeong, D., & Schmidt, F. 2018, *Physics Reports*, 733, 1. <https://doi.org/10.1016/j.physrep.2017.12.002>
- Domínguez-Gómez, J., Lisenfeld, U., Pérez, I., et al. 2022, *A&A*, 658, A124. <https://doi.org/10.1051/0004-6361/202141888>
- Dougllass, K. A., & Vogeley, M. S. 2017, *ApJ*, 834, 186. <https://doi.org/10.3847/1538-4357/834/2/186>
- Dougllass, K. A., Vogeley, M. S., & Cen, R. 2018, *ApJ*, 864, 144. <https://doi.org/10.3847/1538-4357/aad86e>
- Einasto, J., Saar, E., Kaasik, A., & Chernin, A. D. 1974, *Nature*, 252, 111. <https://doi.org/10.1038/252111a0>
- El-Ad, H., & Piran, T. 1997, *ApJ*, 491, 421. <https://doi.org/10.1086/304973>
- El-Badry, K., Wetzel, A. R., Geha, M., et al. 2017, *ApJ*, 835, 193
- Falcón-Barroso, J., Sánchez-Blázquez, P., Vazdekis, A., et al. 2011, *A&A*, 532, A95. <https://doi.org/10.1051/0004-6361/201116842>
- Fall, S. M., & Efstathiou, G. 1980, *MNRAS*, 193, 189. <https://doi.org/10.1093/mnras/193.2.189>
- Ferré-Mateu, A., Durré, M., Forbes, D. A., et al. 2021, *MNRAS*, 503, 5455. <https://doi.org/10.1093/mnras/stab805>
- Florez, J., Berlind, A. A., Kannappan, S. J., et al. 2021, *ApJ*, 906, 97. <https://doi.org/10.3847/1538-4357/abca9f>
- Fraser-McKelvie, A., & Cortese, L. 2022, *ApJ*, 937, 117. <https://doi.org/10.3847/1538-4357/ac874d>
- Frings, J., Macciò, A., Buck, T., et al. 2017, *MNRAS*, 472, 3378. <https://doi.org/10.1093/mnras/stx2171>
- Gardner, J. P., Mather, J. C., Clampin, M., et al. 2006, *SSRv*, 123, 485. <https://doi.org/10.1007/s11214-006-8315-7>
- Goldberg, D. M., & Vogeley, M. S. 2004, *ApJ*, 605, 1. <https://doi.org/10.1086/382143>
- Grcevich, J., & Putman, M. E. 2009, *ApJ*, 696, 385. <https://doi.org/10.1088/0004-637X/696/1/385>
- Grogin, N. A., & Geller, M. J. 1999, *AJ*, 118, 2561. <https://doi.org/10.1086/301126>
- . 2000, *AJ*, 119, 32. <https://doi.org/10.1086/301179>
- Herenz, E. C., Gruyters, P., Orlitova, I., et al. 2016, *A&A*, 587, A78. <https://doi.org/10.1051/0004-6361/201527373>
- Hidalgo, S. L., Pietrinferni, A., Cassisi, S., et al. 2018, *ApJ*, 856, 125. <https://doi.org/10.3847/1538-4357/aab158>
- Hoyle, F., & Vogeley, M. S. 2002, *ApJ*, 566, 641. <https://doi.org/10.1086/338340>
- Hunter, J. D. 2007, *Computing in Science & Engineering*, 9, 90. <https://doi.org/10.1109/MCSE.2007.55>
- Husemann, B., Jahnke, K., Sánchez, S. F., et al. 2013, *A&A*, 549, A87. <https://doi.org/10.1051/0004-6361/201220582>
- Illingworth, G. 1977, *ApJL*, 218, L43. <https://doi.org/10.1086/182572>

- Jarrett, T. H., Masci, F., Tsai, C. W., et al. 2013, *AJ*, 145, 6. <https://doi.org/10.1088/0004-6256/145/1/6>
- Jones, E., Oliphant, T., Peterson, P., & Others. 2001–, *SciPy: Open Source Scientific Tools for Python*, . <https://www.scipy.org/>
- Kallivayalil, N., van der Marel, R. P., Besla, G., Anderson, J., & Alcock, C. 2013, *ApJ*, 764, 161. <https://doi.org/10.1088/0004-637X/764/2/161>
- Kaufmann, T., Wheeler, C., & Bullock, J. S. 2007, *MNRAS*, 382, 1187. <https://doi.org/10.1111/j.1365-2966.2007.12436.x>
- Kazantzidis, S., Mayer, L., Callegari, S., Dotti, M., & Moustakas, L. A. 2017, *ApJL*, 836, L13. <https://doi.org/10.3847/2041-8213/aa5b8f>
- Kazantzidis, S., Lokas, E. L., Callegari, S., Mayer, L., & Moustakas, L. A. 2011, *ApJ*, 726, 98. <https://doi.org/10.1088/0004-637X/726/2/98>
- Kirby, E. N., Bullock, J. S., Boylan-Kolchin, M., Kaplinghat, M., & Cohen, J. G. 2014, *MNRAS*, 439, 1015. <https://doi.org/10.1093/mnras/stu025>
- Kirby, E. N., Rizzi, L., Held, E. V., et al. 2017, *ApJ*, 834, 9. <https://doi.org/10.3847/1538-4357/834/1/9>
- Kniazev, A. Y., Egorova, E. S., & Pustilnik, S. A. 2018, *MNRAS*, 479, 3842. <https://doi.org/10.1093/mnras/sty1704>
- Kreckel, K., Croxall, K., Groves, B., van de Weygaert, R., & Pogge, R. W. 2014, *ApJ*, 798, L15. <https://doi.org/10.1088/2041-8205/798/1/L15>
- Kreckel, K., Platen, E., Aragón-Calvo, M. A., et al. 2012, *AJ*, 16. <https://doi.org/10.1088/0004-6256/144/1/16>
- Kroupa, P. 2000, *MNRAS*, 322, 231. <https://doi.org/10.1046/j.1365-8711.2001.04022.x>
- Lang, D., Hogg, D. W., & Schlegel, D. J. 2016, *AJ*, 151, 36. <https://doi.org/10.3847/0004-6256/151/2/36>
- Law, D. R., Steidel, C. C., Erb, D. K., et al. 2009, *ApJ*, 697, 2057. <https://doi.org/10.1088/0004-637X/697/2/2057>
- Law, D. R., Cherinka, B., Yan, R., et al. 2016, *AJ*, 152, 83. <https://doi.org/10.3847/0004-6256/152/4/83>
- Leaman, R., Venn, K. A., Brooks, A. M., et al. 2012, *ApJ*, 750, 33. <https://doi.org/10.1088/0004-637X/750/1/33>
- Maiolino, R., & Mannucci, F. 2019, *A&A Rv*, 27, 3
- Maraston, C. 2005, *MNRAS*, 362, 799. <https://doi.org/10.1111/j.1365-2966.2005.09270.x>
- Mayer, L., Governato, F., Colpi, M., et al. 2001, *ApJL*, 547, L123. <https://doi.org/10.1086/318898>
- McConnachie, A. W. 2012, *The Astronomical Journal*, 144, 4. <https://doi.org/10.1088/0004-6256/144/1/4>
- McConnachie, A. W., Higgs, C. R., Thomas, G. F., et al. 2021, *MNRAS*, 501, 2363. <https://doi.org/10.1093/mnras/staa3740>
- Mo, H. J., Mao, S., & White, S. D. M. 1998, *MNRAS*, 295, 319. <https://10.1046/j.1365-8711.1998.01227.x>
- Moran, E. C., Shahinyan, K., Sugarman, H. R., Vélez, D. O., & Eracleous, M. 2014, *AJ*, 148, 136. <https://doi.org/10.1088/0004-6256/148/6/136>
- More, S., Diemer, B., & Kravtsov, A. V. 2015, *ApJ*, 810, 36. <https://doi.org/10.1088/0004-637X/810/1/36>
- Morrissey, P., Matuszewski, M., Martin, D. C., et al. 2018, *ApJ*, 864, 93. <https://doi.org/10.3847/1538-4357/aad597>
- O’Sullivan, D., & Chen, Y. 2020, arXiv e-prints, arXiv:2011.05444. <https://ui.adsabs.harvard.edu/abs/2020arXiv201105444O>
- Pan, D. C., Vogeley, M. S., Hoyle, F., Choi, Y.-Y., & Park, C. 2012, *MNRAS*, 421, 926. <https://doi.org/10.1111/j.1365-2966.2011.20197.x>
- Penny, S. J., Brown, M. J. I., Pimblett, K. A., et al. 2015, *MNRAS*, 453, 3519. <https://doi.org/10.1093/mnras/stv1926>
- Pustilnik, S. A., Perepelitsyna, Y. A., & Kniazev, A. Y. 2016, *MNRAS*, 463, 670. <https://doi.org/10.1093/mnras/stw2039>
- Pustilnik, S. A., Tepliakova, A. L., & Kniazev, A. Y. 2011, *Astrophys. Bull.*, 66, 255. <https://doi.org/10.1134/S1990341311030011>
- Pustilnik, S. A., Tepliakova, A. L., & Makarov, D. I. 2019, *MNRAS*, 482, 4329. <https://doi.org/10.1093/mnras/sty2947>
- Putman, M. E., Zheng, Y., Price-Whelan, A. M., et al. 2021, *ApJ*, 913, 53. <https://doi.org/10.3847/1538-4357/ABE391>
- Reines, A. E., Condon, J. J., Darling, J., & Greene, J. E. 2020, *ApJ*, 888, 36. <https://doi.org/10.3847/1538-4357/ab4999>
- Reines, A. E., Greene, J. E., & Geha, M. 2013, *ApJ*, 775, 116. <https://doi.org/10.1088/0004-637X/775/2/116>
- Robitaille, T. P., Tollerud, E. J., Greenfield, P., et al. 2013, *A&A*, 558, A33. <https://doi.org/10.1051/0004-6361/201322068>
- Rosales-Ortega, F. F., Arribas, S., & Colina, L. 2012, *A&A*, 539, A73. <https://doi.org/10.1051/0004-6361/201117774>
- Ruiz-Lara, T., Gallart, C., Beasley, M., et al. 2018, *A&A*, 617, A18. <https://doi.org/10.1051/0004-6361/201732398>
- Salim, S., Lee, J. C., Janowiecki, S., et al. 2016, *ApJS*, 227, 2. <https://doi.org/10.3847/0067-0049/227/1/2>
- Sánchez, S. F., Pérez, E., Sánchez-Blázquez, P., et al. 2016, *RMxAA*, 52, 21. <https://ui.adsabs.harvard.edu/abs/2016RMxAA..52..171S>
- Sánchez-Blázquez, P., Peletier, R. F., Jiménez-Vicente, J., et al. 2006, *MNRAS*, 371, 703. <https://doi.org/10.1111/j.1365-2966.2006.10699.x>

- Sánchez-Janssen, R., Méndez-Abreu, J., & Aguerri, J. A. L. 2010, *MNRAS*, 406, L65.
<https://doi.org/10.1111/j.1745-3933.2010.00883.x>
- Sartori, L. F., Schawinski, K., Treister, E., et al. 2015, *MNRAS*, 454, 3722.
<https://doi.org/10.1093/mnras/stv2238>
- Schlafly, E. F., & Finkbeiner, D. P. 2011, *ApJ*, 737, 103.
<https://doi.org/10.1088/0004-637X/737/2/103>
- Schombert, J. M. 2006, *AJ*, 131, 296.
<https://doi.org/10.1086/497964>
- Simon, J. D., & Geha, M. 2007, *ApJ*, 670, 313.
<https://doi.org/10.1086/521816>
- Spekkens, K., Urbancic, N., Mason, B. S., Willman, B., & Aguirre, J. E. 2014, *ApJ*, 795, 5.
<https://doi.org/10.1088/2041-8205/795/1/L5>
- Teyssier, M., Johnston, K. V., & Kuhlen, M. 2012, *MNRAS*, 426, 1808.
<https://doi.org/10.1111/j.1365-2966.2012.21793.x>
- Tollerud, E. J., Geha, M. C., Grcevich, J., et al. 2016, *ApJ*, 827, 89. <https://doi.org/10.3847/0004-637X/827/2/89>
- Tremonti, C. A., Heckman, T. M., Kauffmann, G., et al. 2004, *ApJ*, 613, 898. <https://doi.org/10.1086/423264>
- van der Wel, A., Noeske, K., Bezanson, R., et al. 2016, *ApJS*, 223, 29
- Vazdekis, A., Coelho, P., Cassisi, S., et al. 2015, *MNRAS*, 449, 1177. <https://doi.org/10.1093/mnras/stv151>
- Wake, D. A., van Dokkum, P. G., & Franx, M. 2012, *ApJL*, 751, L44
- Wegner, G. A., Salzer, J. J., Taylor, J. M., & Hirschauer, A. S. 2019, *ApJ*, 883, 29.
<https://doi.org/10.3847/1538-4357/ab3a3c>
- Westfall, K. B., Cappellari, M., Bershady, M. A., et al. 2019, *AJ*, 158, 231.
<https://doi.org/10.3847/1538-3881/ab44a2>
- Wheeler, C., Pace, A. B., Bullock, J. S., et al. 2017, *MNRAS*, 465, 2420.
<https://doi.org/10.1093/mnras/stw2583>
- White, S. D. M., & Rees, M. J. 1978, *MNRAS*, 183, 341.
<https://doi.org/10.1093/mnras/183.3.341>
- Wright, E. L., Eisenhardt, P. R. M., Mainzer, A. K., et al. 2010, *AJ*, 140, 1868.
<https://doi.org/10.1088/0004-6256/140/6/1868>
- Zhuang, Z., Kirby, E. N., Leethochawalit, N., & de los Reyes, M. A. C. 2021, *ApJ*, 920, 63.
<https://doi.org/10.3847/1538-4357/ac1340>